

See discussions, stats, and author profiles for this publication at: <https://www.researchgate.net/publication/7776161>

The Crystal Structure of Escherichia coli Ketopantoate Reductase with NADP + Bound †, ‡

ARTICLE in BIOCHEMISTRY · JULY 2005

Impact Factor: 3.02 · DOI: 10.1021/bi0502036 · Source: PubMed

CITATIONS

18

READS

24

7 AUTHORS, INCLUDING:



Alessio Ciulli

University of Dundee

57 PUBLICATIONS 782 CITATIONS

SEE PROFILE



Alison G Smith

University of Cambridge

170 PUBLICATIONS 4,560 CITATIONS

SEE PROFILE



Chris Abell

University of Cambridge

294 PUBLICATIONS 8,060 CITATIONS

SEE PROFILE



Tom L Blundell

University of Cambridge

652 PUBLICATIONS 38,743 CITATIONS

SEE PROFILE

The Crystal Structure of *Escherichia coli* Ketopantoate Reductase with NADP⁺ Bound^{†,‡}

Carina M. C. Lobley,[§] Alessio Ciulli,^{||} Heather M. Whitney,[⊥] Glyn Williams,[#] Alison G. Smith,[⊥] Chris Abell,^{||} and Tom L. Blundell^{*,§}

Department of Biochemistry, University of Cambridge, 80 Tennis Court Road, Cambridge CB2 1GA, U.K., University Chemical Laboratory, Lensfield Road, Cambridge CB2 1EW, U.K., Department of Plant Sciences, University of Cambridge, Downing Street, Cambridge CB2 3EA, U.K., and Astex Technology Ltd., 436 Cambridge Science Park, Milton Road, Cambridge CB4 0QA, U.K.

Received February 3, 2005; Revised Manuscript Received April 29, 2005

ABSTRACT: The NADPH-dependent reduction of ketopantoate to pantoate, catalyzed by ketopantoate reductase (KPR; EC 1.1.1.169), is essential for the biosynthesis of pantothenate (vitamin B₅). Here we present the crystal structure of *Escherichia coli* KPR with NADP⁺ bound, solved to 2.1 Å resolution. The cofactor is bound in the active site cleft between the N-terminal Rossmann-fold domain and the C-terminal α-helical domain. The thermodynamics of cofactor and substrate binding were characterized by isothermal titration calorimetry. The dissociation constant for NADP⁺ was found to be 6.5 μM, 20-fold larger than that for NADPH (0.34 μM). The difference is primarily due to the entropic term, suggesting favorable hydrophobic interactions of the more lipophilic nicotinamide ring in NADPH. Comparison of this binary complex structure with the previously studied apoenzyme reveals no evidence for large domain movements on cofactor binding. This observation is further supported both by molecular dynamics and by calorimetric analysis. A model of the ternary complex, based on the structure presented here, provides novel insights into the molecular mechanism of enzyme catalysis. We propose a conformational switch of the essential Lys176 from the “resting” state observed in our structure to an “active” state, to bind ketopantoate. Additionally, we identify the importance of Asn98 for substrate binding and enzyme catalysis.

Pantothenate biosynthesis in *Escherichia coli* requires four enzymes to convert α-ketoisovalerate (α-KIVA) and L-aspartate to pantothenate (1–3). The second reaction in this biosynthetic pathway is the NADPH-dependent reduction of ketopantoate to pantoate, catalyzed by ketopantoate reductase (KPR;¹ EC 1.1.1.169) (4–7). The subsequent condensation of pantoate with β-alanine gives rise to pantothenate (vitamin B₅), the universal precursor to the phosphopantetheine moiety of coenzyme A and acyl carrier protein (2, 3).

Ketopantoate reductase, encoded by the *panE* gene, has been characterized from *E. coli*, *Salmonella typhimurium*,

and *Pseudomonas maltophilia* 845 (7–14). Although KPR from *P. maltophilia* 845 is reported to be multimeric, consisting of three to five subunits each with a molecular mass of 30 kDa (8), recombinant KPR from *E. coli* and *S. typhimurium* are homologous, monomeric proteins, with a molecular mass of 34 kDa (9, 10, 12, 15). *E. coli* KPR catalyzes the stereospecific transfer of the *pro-S* hydride of NADPH to the *si* face of ketopantoate, via an ordered sequential bi–bi mechanism (12). The pH dependence of catalysis is consistent with the involvement of a general acid/base in the catalytic mechanism (12). Analysis of the activity of several site-directed mutants of KPR implicated both Lys176 and Glu256 in the catalytic mechanism (11). Analysis of the crystal structure of KPR confirmed the presence of these residues in the active site and led to the proposal that Glu256 was the required general acid/base and that Lys176 stabilized substrate binding (14).

In this paper we present the three-dimensional structure of the complex of KPR with NADP⁺, solved to 2.1 Å resolution. This structure and additional data obtained from binding studies and site-directed mutagenesis have been used to establish the nature and location of the active site of KPR and to further our understanding of its catalytic mechanism.

MATERIALS AND METHODS

Ketopantoate and pantoate were prepared by hydrolysis of their respective lactones as described elsewhere (5).

[†] This work was supported by BBSRC Grant 8/B15141. C.M.C.L. is funded by the BBSRC; A.C. is funded by Astex Technology Ltd., BBSRC, and the Gates Cambridge Trust.

[‡] Atomic coordinates have been deposited with the Protein Data Bank with the PDB code 1YJQ.

* Corresponding author. Telephone: 01223 333629. Fax: 01223 766082. E-mail: tom@cryst.bioc.cam.ac.uk.

[§] Department of Biochemistry, University of Cambridge.

^{||} University Chemical Laboratory.

[⊥] Department of Plant Sciences, University of Cambridge.

[#] Astex Technology Ltd.

¹ Abbreviations: CPMG, Carr–Purcell–Meiboom–Gill; HEPES, 4-(2-hydroxyethyl)-1-piperazineethanesulfonic acid; IPTG, isopropyl thio-β-D-galactoside; ITC, isothermal titration calorimetry; KPR, ketopantoate reductase; MPD, 2-methyl-2,4-pentanediol; NADP⁺, oxidized nicotinamide adenine dinucleotide phosphate; NADPH, reduced nicotinamide adenine dinucleotide phosphate; NMR, nuclear magnetic resonance; PMSF, phenylmethanesulfonyl fluoride; PNAC, Protein and Nucleic Acid Chemistry Facility (Cambridge); SASA, solvent-accessible surface area; Water-LOGSY, water–ligand observed via gradient spectroscopy.

Protein Expression and Purification. The *panE* gene encoding *E. coli* KPR, cloned into pET24b, was used to overexpress KPR in *E. coli* BL21(DE3) cells as described elsewhere (14). Alternatively, the 915 bp *panE* gene was subcloned into the pRSETa vector (Invitrogen) to allow expression of KPR with an N-terminal His₆ tag. In this case *E. coli* C41(DE3) cells were used as host cells.

E. coli were grown in LB broth, supplemented with kanamycin to a final concentration of 25 µg/mL (pET24b), or ampicillin to a final concentration of 100 µg/mL (pRSETa), at 37 °C to OD_{600nm} = 0.6. Expression was induced with isopropyl β-D-thiogalactoside (IPTG) at a final concentration of 400 µM. After 4 h incubation, cells were harvested by centrifugation. The resulting cell pellets, containing either KPR or His₆-KPR, were resuspended in 10 mM Bicine, pH 8.0, or 10 mM potassium phosphate, pH 8.0, 10 mM imidazole, and 300 mM NaCl, respectively. Buffers included 0.007% (v/v) of β-mercaptoethanol, 0.2 mg/mL lysozyme, 1 mM PMSF, and 0.5% (v/v) of protease inhibitor cocktail (Sigma). Cells were lysed using high pressure or by sonication, for a total process time of 3 min, followed by centrifugation.

To purify native KPR, the filtered cell lysate was applied to a 25 mL Q-Sepharose anion-exchange column and eluted with a salt gradient to 1 M NaCl in 10 mM Bicine, pH 8.0. After buffer exchange to 50 mM potassium phosphate, pH 7.5, fractions containing KPR were applied to a 5 mL blue Sepharose column and eluted with a salt gradient to 1 M KCl. The final step in the purification was gel filtration, using a Superdex 200, 26:60 gel filtration column in 10 mM HEPES, pH 8.0. All columns were purchased from Amersham Pharmacia. Peaks containing KPR were identified by SDS-PAGE (16). The final purity and identity of KPR was confirmed using mass spectrometry and N-terminal sequencing (Protein and Nucleic Acids Facility, University of Cambridge). Purified KPR was concentrated using a Vivaspinn 10 kDa cutoff centrifugal concentrator.

His₆-KPR was applied to a Ni-NTA column (Qiagen), preequilibrated with 10 mM potassium phosphate, pH 8.0, 10 mM imidazole, and 300 mM NaCl. After the column was washed with this buffer containing 50 mM imidazole, the protein was eluted with 250 mM imidazole. Fractions containing KPR, as assessed by SDS-PAGE, were pooled and exchanged into the appropriate buffer for binding studies.

Protein concentration was determined by A_{280nm}, using an estimated absorption coefficient for KPR of 47870 M⁻¹ cm⁻¹ calculated from the sequence. An absorption coefficient of 62650 M⁻¹ cm⁻¹ was obtained from amino acid analysis of His₆-KPR by the Protein and Nucleic Acid Chemistry Facility (PNAC), Department of Biochemistry, University of Cambridge.

Crystallization of KPR. Crystal trials were carried out using vapor diffusion by the hanging drop method (17), using a protein concentration of 10–15 mg/mL. Prior to crystallization KPR samples were incubated at 4 °C with NADP⁺ and ketopantoate. The ratio of NADP⁺ to protein was 2:1, and that of ketopantoate to protein was 5:1. Needlelike crystals of KPR were obtained in 10% 2-methyl-2,4-pentanediol (MPD) buffered with 0.1 M NaOAc, pH 4.0–5.0. To facilitate data collection at 100 K, these crystals were cryoprotected in 30% MPD buffered with 0.1 M NaOAc at the same pH as the well solution.

Table 1: Statistics for KPR Data Collection and Refinement

Data Collection	
X-ray source	SRS (14.2)
space group	<i>P</i> ₂ ₁ ₂ ₁ ₂ ₁
cell parameters, Å	<i>a</i> = 60.83
(α = β = γ = 90°)	<i>b</i> = 66.14
	<i>c</i> = 98.81
wavelength, Å	0.979
resolution range, Å (outer shell)	30–2.1 (2.15–2.10)
no. of unique reflections	24200
multiplicity	6.45
<i>R</i> _{merge} (outer shell)	9.2 (43.6)
average <i>I</i> /σ <i>I</i> (outer shell)	14.0 (3.2)
% reflections with <i>I</i> /σ <i>I</i> > 3 (outer shell)	72 (43.0)
completeness, % (outer shell)	99.7 (99.9)
mosaicity, deg	0.24
Wilson <i>B</i> , Å ²	23.4
Refinement	
<i>R</i> _{cryst} , ^a %	16.0
<i>R</i> _{free} , ^b %	19.4
no. of reflections	
working set	22838
test set	1231
no. of residues rebuilt	293
Model Quality	
estimated coordinate error, ^c Å ²	0.14
Ramachandran plot, ^d %	
most favored	98.3
generously allowed	1.7
disallowed	0
rmsd bonds, ^c Å	0.02
rmsd angles, ^c deg	1.90
overall mean <i>B</i> , ^c Å ²	22.6

^a *R*_{cryst} = Σ||*F*_o| - |*F*_c||/Σ|*F*_o|, where *F*_o and *F*_c are observed and calculated structure factor amplitudes. ^b *R*_{free} as for *R*_{cryst} using a random subset of the data excluded from the refinement. ^c Estimated coordinate error based on the free *R*-value as calculated by Refmac (21, 24). ^d Calculated with Rampage (47).

X-ray Data Collection, Crystal Structure Determination, and Refinement. X-ray data to 2.1 Å resolution were collected at station 14.2, SRS Daresbury. The principal parameters and data statistics for these data collection are shown in Table 1. Denzo and Scalepack, from the HKL200 suite (18), were used to process the data. The structure was solved using AMoRe, from the CCP4 suite (19–21), to carry out molecular replacement, with apo KPR as the probe structure.

Following molecular replacement, simulated annealing was carried out using CNS, and initial electron density maps were produced (22). The structure was refined using successive rounds of manual rebuilding in XtalView (23) and maximum likelihood refinement using Refmac 5 from the CCP4 suite (21, 24). The final structure includes residues 1–293 of KPR in complex with one molecule of bound NADP⁺. In addition, 1 molecule of MPD and 1 molecule of acetate have been included in the modeled solvent. Coordinates for the non-protein molecules were obtained from the HiCUP database (25), and refinement libraries were obtained from the Prodrgr server (26).

Functional Complementation. Seven site-directed mutants (K72A, N98A, K176A, E210A, S244A, D248A, and E256A) of the *panE* gene cloned in pET24b were made using the QuickChange kit (Stratagene). The primers are listed in Table 2. The *panE* coding sequences were then subcloned to pBADMyHisB (Invitrogen) using PCR with the primers in Table 2. In addition, N98A was made in *panE* cloned in pRSETa. The activity of these mutants was tested *in vivo*

Table 2: Primers Used for Cloning and Mutagenesis

Purpose	Primers	
Subcloning pBADmycHisB	Forward	CTA AGG ACC ATG GCA ATT ACC GTA TTG GGA TGG
	Reverse	GCC TAG AAG CTT CTA CCA GGG GCG AGG CAA ACC
K72A	Forward	CTG GTG ACG CTG GCA GCA TGG CAG GTT TCC
	Reverse	GGA AAC CTG CCA TGC TGC CAG CGT CAC CAG
N98A	Forward	CCA ATA CTG TTA ATT CAC GCG GGC ATG GGC ACC
	Reverse	GGT GCC CAT GCC CGC GTG AAT TAA CAG TAT TGG
K176A	Forward	GAG CTG TGG CGC GCG CTG GCA GTC AAC TGC
	Reverse	GCA GTT GTC TGC CAG CGC GCG CCA CAG CTC
E210A	Forward	CAG ATA TGC GAA GCA GTC GCG GCG GTG ATC
	Reverse	GAT CAC CGC CGC GAC TGC TTC GCA TAT CTG
S244A	Forward	GCG GAA AAT ATC TCG GCG ATG TTG CAG GAT ATC CGC
	Reverse	GCG GAT ATC CTG CAA CAT CGC CGA AGT ATT TTC CGC
D248A	Forward	CGA TGT TGC AGG CTA TCC GCG CGG CGC TGC
	Reverse	GCA GCG CCG CGC GGA TAG CCT GCA ACA TCG
E256A	Forward	GCG CTG CGC CAC ACT GCA ATC GAC TAT ATC
	Reverse	GAT ATA GTC GAT TGC AGT GTG GCG CAG CGC
N98A (in pRSETa)	Forward	CGC CAA TAC TGT TAA TTC ACG CAG GCA TGG GCA
	Reverse	TGC CCA TGC CTG CGT GAA TTA ACA GTA TTG GCG

using a *panE*⁻/*ilvC*⁻ double knock-out strain of *S. typhimurium*, DM 3498 (10). This strain cannot grow on minimal media unless it is supplemented with the branched-chain amino acids and either pantoate or pantothenate. Cells were transformed with pBADMyHisB carrying one of the mutated *panE* genes and grown on minimal media in the absence of pantoate or pantothenate to determine the functional competence of the expressed, mutated KPR protein.

NMR Spectroscopy. All NMR spectra were recorded at 298 K on a Bruker DRX 500 MHz spectrometer equipped with a 5 mm triple resonance inverse (TXI) cryoprobe with Z-gradients. All NMR samples for ligand binding studies contained 1 mM ligand, 50 μ M enzyme, 20 mM potassium phosphate buffer, pH 7.2, 80 mM NaCl, and 10% D₂O. Control experiments were carried out using samples where the enzyme was omitted. For calibration, trimethylsilyl-propionic acid-*d*₄ (TSP) (20 μ M) was present in all samples and as a control in Carr–Purcell–Meiboom–Gill (CPMG) (27) experiments. Water suppression was achieved by using a 1.6 s presaturation pulse and a WATERGATE (WATER suppression by gradient-tailored excitation) (28) gradient spin–echo sequence. Relaxation-edited NMR experiments incorporated a CPMG spin-lock time of 200–400 ms before the acquisition period. Water-LOGSY (water–ligand observed via gradient spectroscopy) (29) NMR experiments employed a 20 ms selective Gaussian 180° pulse at the water signal frequency and an NOE mixing time of 1 s.

Isothermal Titration Calorimetry. Isothermal titration calorimetry (ITC) experiments were performed on an OMEGA isothermal titration calorimeter from Microcal Inc. at 27 °C. Details of instrumentation and experimental design are described elsewhere (30). Purified protein was exhaustively dialyzed with 100 mM HEPES, pH 7.6. Nucleotide cofactors were dissolved in the same buffer and their concentrations determined by UV spectrophotometry. A typical experiment

used 30–50 μ M enzyme in the sample cell (1.345 mL). Injections of 7.0–8.0 μ L of a 400–600 μ M cofactor solution were added from a 300 μ L syringe rotating at 300 rpm. Typically, 35 injections of 8 s duration were made at 3–4 min intervals.

Titration of ketopantoate and pantoate were conducted using low *c*-value experimental conditions (31). Sufficient ligand was used to obtain at least 80% saturation of the enzyme at the end of the titration, as estimated using the equation described by Turnbull and Daranas (31). Typically, the initial 14 injections were of 3–4 μ L, and the final 30 injections were of 7–8 μ L, all at 3–4 min intervals. The heat change accompanying the titration was recorded as differential power by the instrument and determined by integration of the peak obtained. Titrations of ligand to buffer only were performed to allow baseline corrections. Nonlinear least-squares minimization was used to obtain the dissociation constant, *K*_d, the enthalpy of binding, ΔH , and the stoichiometry, *n* (30). A stoichiometry of 1, determined from titrations with NADP(H), was fixed during curve fitting of data obtained under low *c*-value conditions.

Molecular Dynamics Simulations. Molecular dynamics simulations were carried out using the Dynamite (32) and El Nemo (33) programs. These programs are run by dedicated web servers and accessed via http://s12-ap550.biop.ox.ac.uk/dynamite_html and <http://igs-server.cnrs-mrs.fr/~suhre/NMODE/index.html>, respectively.

Surface Area Calculations. The solvent-accessible surface areas (SASAs) and their relative polar and apolar contributions were calculated by the program GETAREA 1.1 (34) using the crystal structure presented here. The surface buried upon complex formation with NADP⁺ was determined as the difference between the SASA of the complex and the sum of the surface areas of NADP⁺ and after removal of the nucleotide cofactor.

RESULTS AND DISCUSSION

Overexpression, Purification, and Crystallization. A 1 L culture was sufficient to obtain 7–10 mg of purified native KPR enzyme via a three-step chromatographic purification strategy. A one-step purification strategy was sufficient to obtain 30–50 mg of His₆-KPR from a 1 L culture. The protein behaved as a monomer in gel filtration, and its identity was confirmed by SDS–PAGE, N-terminal sequencing, and mass spectrometry (data not shown).

Initial attempts to crystallize the complex between KPR, NADP⁺, and ketopantoate explored conditions similar to those used for the apo KPR crystals (28–38% PEG 4000, 0.1 M Tris, pH 9.4, and 0.25 M NaOAc) (14). As a result of sparse matrix screening, small, needlelike crystals were identified in solution 1 of Crystal Screen Lite (Hampton Research). These conditions were optimized to those given in the Materials and Methods. This gave clusters of larger needlelike crystals, from which single crystals could be dissected.

Structure Solution and Refinement. The crystal structure of the KPR–NADP⁺ complex was solved using molecular replacement in AMoRe (19–21). The first solution, with an *R*-factor of 21.4% and a correlation coefficient of 56.0%, was used. After simulated annealing, the $2F_o - F_c$ and F_o

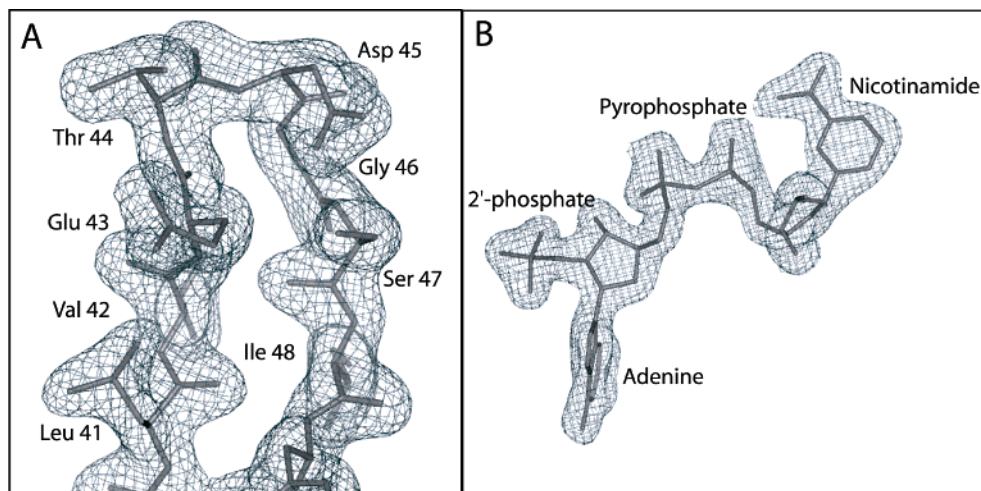


FIGURE 1: Electron density from the KPR structure. Panel A shows a typical section of electron density from the final $2F_o - F_c$ map. Panel B shows same map in the region of the active site. This electron density clearly indicates the presence and orientation of NADP⁺. In both diagrams the map is contoured at 1σ .

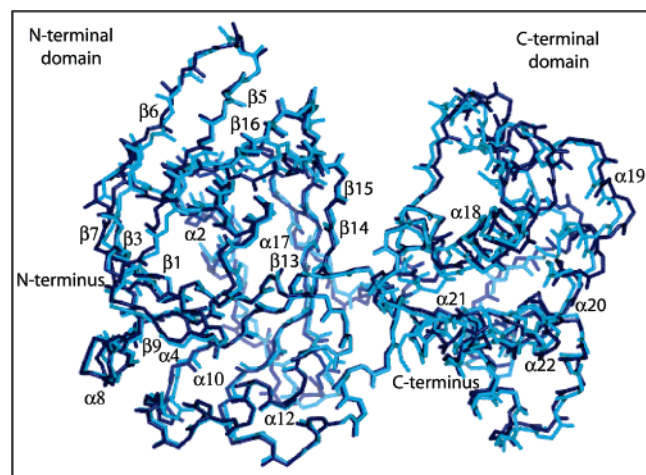


FIGURE 2: Superposition of apo KPR and the KPR binary structures. Comparison of apo KPR (1KS9), dark blue, and the binary complex (1YJQ), cyan. The protein structures were superposed using the main chain atoms of residues 1–169 (the N-terminal domain).

— F_c electron density maps clearly showed the position of NADP⁺ within the active site cleft of KPR. Accordingly, a molecule of NADP⁺ was modeled in this electron density. Unfortunately, no ketopantoate was identified, either in the active site or nonspecifically bound in the solvent shell. Subsequent ITC binding experiments revealed that KPR binds ketopantoate weakly (K_d 10 mM) in the presence of a saturating concentration of NADP⁺.

Maximum likelihood refinement, using Refmac 5 (21, 24), was used to improve the quality of the electron density maps and facilitate further rebuilding and improvement of the molecular model, until no unexplained electron density remained, and the R_{cryst} and R_{free} values converged at 16.0% and 19.4%, respectively (Figure 1). The C-terminal 10 residues were disordered in the electron density and were not rebuilt. This reflects the situation in the apo crystal structure where the C-terminal 12 residues are disordered (14).

The Binary Complex Structure of KPR. The binary complex of KPR has the same overall structure as the apoenzyme (14) (Figure 2). The NADP⁺ molecule is located in a cleft between the N-terminal Rossmann-fold domain and

the C-terminal α -helical domain and is capable of forming hydrogen bonds to both domains (Figure 3A).

The GXGXXG motif, common to nucleotide binding proteins (35, 36), is involved in a tight turn, allowing interactions between the pyrophosphate in NADP⁺ and the backbone amides of Ala10 and Leu11. The other main interactions between the protein and cofactor are a hydrophobic pocket, to accommodate the adenine moiety, defined by the aliphatic moieties of the side chains of Arg31, Leu71, and Gln75; hydrogen bonds between Arg31 and the 2'-ribose phosphate; hydrogen bonds from Asn98 and Glu256 to the nicotinamide ribose 2'- and 3'-hydroxyls; and hydrogen bonds between the backbone amide and carbonyl of Ala122 with the substituent carboxyl and amide groups of the nicotinamide ring (Figure 3A). Interestingly, Lys72, which was proposed by Matak-Vinkovic et al. (14) to have a role in cofactor binding, is not oriented toward the cofactor. This is consistent both with the observation that mutating Lys72 to alanine does not affect the turnover of NADPH in cell lysate (11) and with the results of the functional study presented herein. Reorientation of the side chain of Lys72 might facilitate hydrogen bonding to the pyrophosphate of NADP⁺ although the terminal amino group is involved in an interdomain hydrogen bond to another strictly conserved residue, Asp248.

NMR Spectroscopy. The formation of binary complexes of KPR with the cofactors NADPH and NADP⁺ and the substrates ketopantoate and pantoate was investigated using one-dimensional ¹H NMR spectroscopy. Water-LOGSY and CPMG experiments were used to detect binding of ligands to KPR by comparing their NMR signals in the presence and absence of the protein. In Water-LOGSY, compounds that bind to the protein show positive signals due to cross-relaxation from water (29). In a CPMG experiment, the ligand signals in the presence of the protein have lower intensities, compared with those in its absence, due to a decrease in their transverse relaxation times (T_2) (37). The binding of both NADPH and NADP⁺ to apo KPR was detected using these NMR experiments. In addition, 1 mM pantoate was observed to bind to KPR (Figure 4, right) whereas no binding of ketopantoate was detected at the same

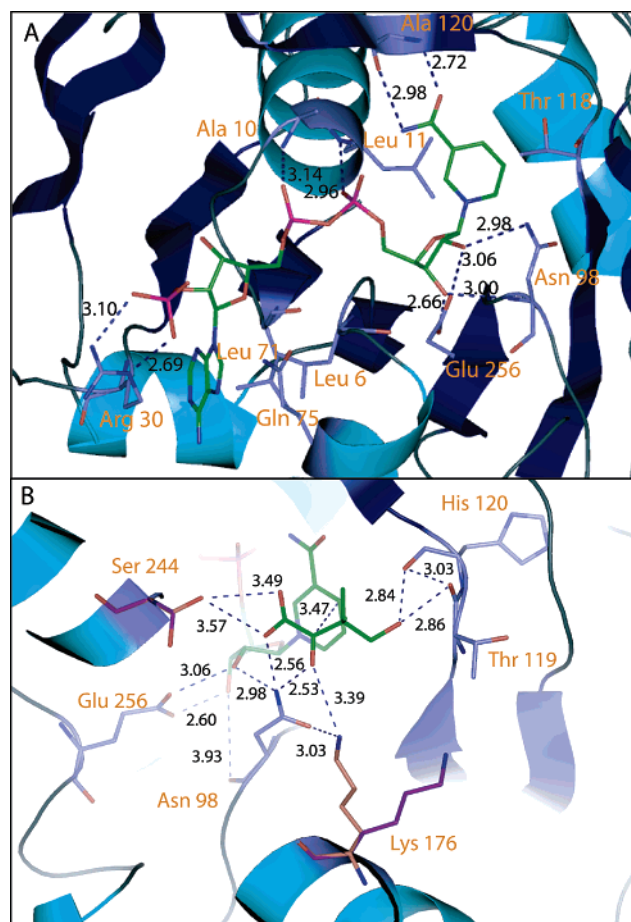


FIGURE 3: The NADP⁺ complex and modeled ternary complex with ketopantoate. (A) The complete binding site for NADP⁺. The cofactor is displayed with green carbons, while key side chains have blue carbons. Side chains are labeled in orange, and interatomic distances are given in black. (B) The predicted binding of ketopantoate in the active site of the binary complex. The side chains of Lys176 and Ser244 have been moved to produce this model; their new positions are displayed with pink carbons while the observed positions are in purple.

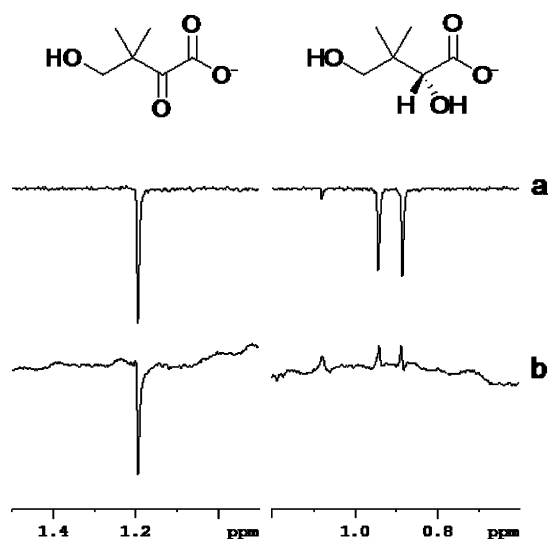


FIGURE 4: NMR binding experiments. The water-LOGSY NMR spectra for 1 mM ketopantoate (a) alone and (b) in the presence of 50 μ M KPR are shown on the left. On the right the corresponding experiments for pantoate are shown.

concentration (Figure 4, left) either to KPR or to the KPR–NADP⁺ complex. In these experiments His₆-KPR was used.

This form of the enzyme is catalytically active and has kinetic parameters comparable to those of the native enzyme.

Isothermal Titration Calorimetry. The thermodynamics of binding of cofactors and substrates to His₆-KPR were determined using ITC (Table 3). Results for titration experiments of NADPH and NADP⁺ are shown in Figure 5. The dissociation constant for NADPH was $0.34 \pm 0.02 \mu$ M. Interestingly, our value is about 6 times lower than that reported by Zheng and Blanchard (13) using ITC under similar conditions. The binding of NADP⁺ was about 20-fold weaker than that of NADPH ($K_d = 6.5 \pm 0.6 \mu$ M), as can be appreciated by a comparison of the slopes of the two curves in Figure 5. Binding of NADPH and NADP⁺ is favored both entropically and enthalpically. ΔH values are comparable (-3.2 kcal/mol), while ΔS is more favorable for NADPH ($T\Delta S = 5.7$ kcal/mol) than for NADP⁺ ($T\Delta S = 4$ kcal/mol). This entropic term accounts for the more favorable free energy of binding of the reduced form of the cofactor compared to the oxidized form. This is possibly due to favorable hydrophobic interactions with the enzyme active site of the more lipophilic nicotinamide ring of NADPH. The crystal structure shows that the nicotinamide group sits in a predominantly hydrophobic pocket (Figure 6).

The binding of ketopantoate and pantoate to His₆-KPR was detected by ITC. Binding of ketopantoate was weak, with a dissociation constant of 5.3 ± 0.1 mM. The substrate bound even more weakly in the presence of a saturating concentration of NADP⁺. This low affinity explains the absence of ketopantoate in the X-ray structure and the inability to detect ketopantoate binding by NMR spectroscopy. Pantoate ($K_d = 270 \pm 10 \mu$ M) binds 20-fold more tightly than ketopantoate, which is interesting given their structural similarity. Binding of both ketopantoate and pantoate is primarily enthalpic (-5.6 and -8.1 kcal/mol, respectively). It is interesting to note that the K_d for ketopantoate dissociation from KPR (as measured by ITC) is 5.3 mM, while the K_m value for ketopantoate binding the binary KPR–NADPH complex is 0.12 mM (12). This observation is consistent with ketopantoate binding following NADPH binding in the ordered sequential kinetic mechanism reported for KPR (12).

Hinge Bending. The failure to soak ligands into preformed crystals of KPR had previously been thought to be due to an associated hinge bending, which could not be accommodated in the crystal lattice. Such domain movements have been observed for other dehydrogenases (38–42). However, comparison of the structure of KPR and the KPR–NADP⁺ complex, by superposition of main chain atoms of the N-terminal domains, shows that there are no large domain movements associated with cofactor binding. The overall main chain rms deviation between the structures is 0.98 Å (Figure 2).

We investigated the idea of “protein breathing” using normal mode molecular dynamics simulations (43). The results of this analysis show the potential for a twisting movement between the domains, which would result in a subtle opening and closing of the active cleft of KPR (Supporting Information). This proposed movement would be sufficient to enable the cofactor to enter and leave the active site. However, no single region is identified as a “hinge” region.

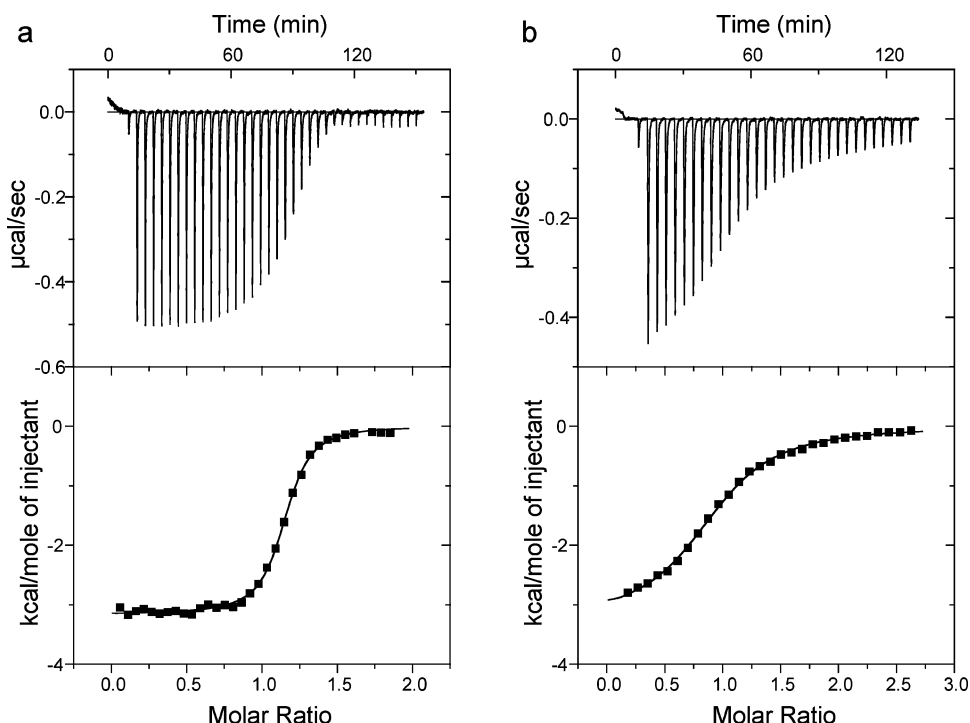


FIGURE 5: Typical ITC titrations of KPR. The upper panels give raw data for the titration of 50 μ M KPR titrated with (a) 500 μ M NADPH and (b) 680 μ M NADP⁺. With the exception of the first peak, peaks correspond to 7 μ L injections. The lower panels give the integrated curve, fitted with the ORIGIN program using a one-site model.

Table 3: Thermodynamic Parameters of Cofactor and Substrate Binding to *E. coli* KPR

ligand	K_d (μ M)	ΔG (kcal/mol)	ΔH (kcal/mol)	$-T\Delta S$ (kcal/mol)
NADPH	0.34 ± 0.02	-8.89 ± 0.03	-3.16 ± 0.01	-5.73 ± 0.04
NADP ⁺	6.5 ± 0.6	-7.13 ± 0.05	-3.15 ± 0.06	-3.97 ± 0.08
ketopantoate	5300 ± 70	-3.13 ± 0.01	-5.6 ± 0.1	-2.5 ± 0.1
pantoate	270 ± 10	-4.91 ± 0.02	-8.1 ± 0.2	-3.2 ± 0.2

In addition to this structural and computational analysis, the proposal of hinge bending was assessed using ITC. Titrations of NADPH and NADP⁺ into His₆-KPR were performed at 17, 27, and 37 °C. The ΔH and $T\Delta S$ terms were found to depend strongly on temperature. However, ΔG remained almost constant due to enthalpy–entropy compensation (44). Values of ΔC_p were calculated from the slope of the regression lines of ΔH versus temperature, assuming a constant heat capacity change in the investigated temperature range. ΔH was found to decrease with increasing temperature, resulting in negative heat capacity ΔC_p changes of -210 and -180 cal K⁻¹ mol⁻¹ for NADPH and NADP⁺, respectively.

In protein–ligand interactions, the heat capacity change associated with complex formation has been shown to correlate with the amount and type of solvent-accessible surface area (SASA) buried in the complex, according to the equation (45):

$$\Delta C_p = (0.32 \pm 0.04)\Delta \text{SASA}_{\text{np}} - (0.14 \pm 0.04)\Delta \text{SASA}_{\text{p}} \quad \text{cal mol}^{-1} \text{K}^{-1} \quad (1)$$

in which $\Delta \text{SASA}_{\text{np}}$ and $\Delta \text{SASA}_{\text{p}}$ are changes in water-accessible nonpolar and polar surface area, respectively.

Changes in SASA can be calculated by removing NADP⁺ from the binary complex crystal structure. Since this is not strictly the apo form of the enzyme, such calculation will correspond to a rigid body model that assumes no confor-

mational changes take place upon cofactor binding. From the ΔSASA calculated this way, one can extrapolate ΔC_p according to eq 1 (45) and then compare it to the value measured experimentally from the temperature-dependent calorimetric experiments. If the experimental ΔC_p is very different from the calculated value, this would suggest the occurrence of major conformational changes in the protein structure upon ligand binding, as has been previously noted in systems known to undergo large conformational rearrangements (45), such as ATP binding to thymidine kinase (46).

From the binary complex structure of KPR and NADP⁺, $\Delta \text{SASA}_{\text{np}}$ and $\Delta \text{SASA}_{\text{p}}$ were calculated as 760 and 360 Å², respectively. From eq 1 this corresponds to a theoretical ΔC_p of -190 cal mol⁻¹ K⁻¹. This value is in good agreement with the experimentally derived values for both NADPH and NADP⁺ (ΔC_p of -210 and -180 cal mol⁻¹ K⁻¹, respectively). Although there is the possibility of a balance between polar and nonpolar surface, such that ΔC_p would not be expected to change significantly with cofactor-induced conformational changes in solution, we view this as unlikely. Such correlation therefore renders unlikely the occurrence of large conformational changes or hinge bending upon cofactor binding, in support of both the structural and the molecular dynamics analysis.

Functional Analysis of KPR Mutants. A series of site-directed mutants of KPR (K72A, N98A, K176A, E210A,

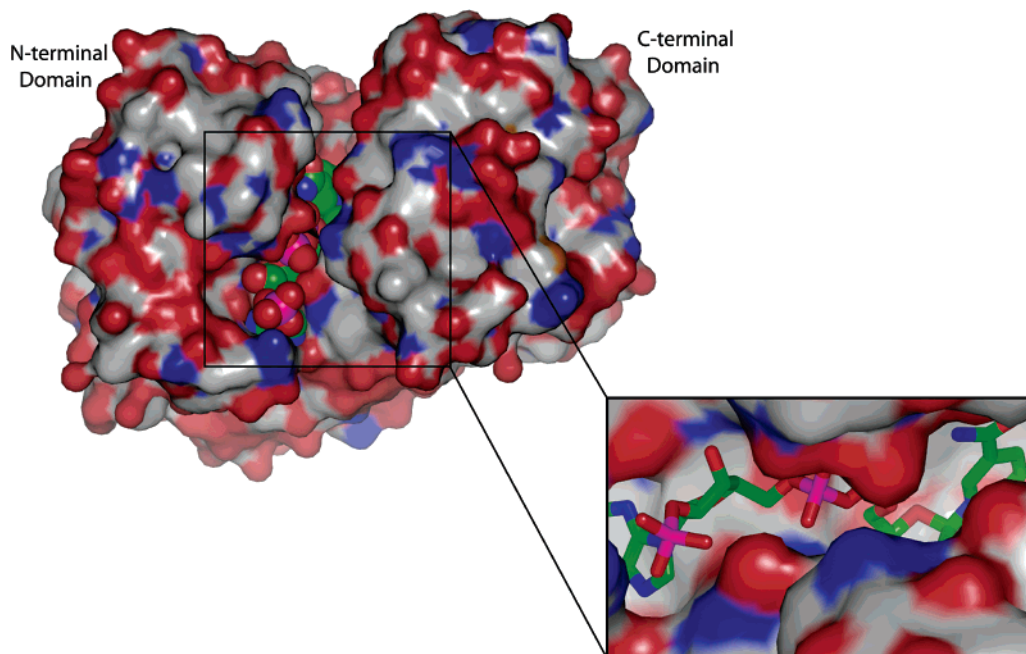


FIGURE 6: van der Waals surface representation of the KPR binary complex. The van der Waals surface of KPR is shown, colored by atom type (carbon, white; oxygen, red; nitrogen, blue). The magnified image reveals the deep cleft into which NADP⁺ binds and the hydrophobic pocket surrounding the nicotinamide ring. For clarity the carbons of the NADP⁺ molecule are colored green.

S244A, D248A, and E256A) were generated to probe the role of specific conserved residues close to the active site. Functional complementation was used to determine the ability of these seven mutants to rescue an *ilvC*, *panE* mutant of *S. typhimurium*, dependent on pantoate for growth. K72A, E210A, S244A, and D248A were all able to complement the mutant, whereas the cells containing mutations to Asn98, Lys176, and Glu256 were unable to survive on minimal media (data not shown). Five conserved residues (Lys72, Lys176, Glu210, Asp248, and Glu256) had been previously mutated to Ala (11). Of these, the K176A and E256A mutant proteins were purified and characterized kinetically. They showed approximately 78000- and 2600-fold decreases in k_{cat}/K_m for ketopantoate, respectively (11). The other three mutant proteins were assayed in crude cell lysates and displayed essentially wild-type activity. The functional study presented here is consistent with these analyses.

The functional complementation experiments indicated Asn98 is also involved in the catalytic mechanism. Further investigations were conducted to confirm the involvement of Asn98 in the kinetic mechanism and to characterize the N98A mutant. The N98A mutant enzyme showed about 50-fold decrease in k_{cat} and 83-fold increase in K_m for ketopantoate, with an overall decrease of about 4000-fold in k_{cat}/K_m . Attempts to detect ketopantoate and pantoate binding to the N98A mutant enzyme by ITC were unsuccessful as no heat effect was observed. These results suggest that Asn98 is important for both catalysis and substrate binding.

The Ternary Complex and Molecular Mechanism of KPR. Ketopantoate (Figure 3b) and pantoate were separately modeled in the active site of the KPR–NADP⁺ structure. The orientation of the substrate/product took into account the known stereospecificity of the catalytic reaction. The conformations of the side chains of Lys176 and Ser244 were altered in order to maximize the potential hydrogen bonding to the substrate. In this model of the ternary complex, several interactions are involved in binding ketopantoate. Ser244 and

Asn98 hydrogen bond to the C1 carboxylic acid, Asn98 and Lys176 interact with the C2 carbonyl, and the C4 hydroxyl hydrogen bonds to the backbone carbonyls of both Thr119 and His120 (Figure 3B). In addition to these interactions with the enzyme, ketopantoate can interact with the nicotinamide ring of the cofactor. This may provide further explanation for the ordered kinetic mechanism previously characterized (12). The resulting models were energy minimized using Sybyl (Tripos).

This model supports the crucial roles played by Asn98, Lys176, and Glu256. Zheng et al. (11, 12) proposed that Lys176 was involved in catalysis and in substrate binding, acting as a general acid in the direction of ketopantoate reduction. In the same work (11) Glu256 was proposed to be crucial through potential interactions with the C4 alcohol of ketopantoate and pantoate (Figure 7A). The mechanism proposed by Matak-Vinkovic et al. (14), based on the additional information obtained from the crystal structure of the apoenzyme, implied that Glu256 acted indirectly as the general acid/base for catalysis. In this proposal Lys176 was required to stabilize ketopantoate and pantoate binding (Figure 7B).

The model of the ternary complex based on the current KPR–NADP⁺ structure provides additional insight into the catalytic mechanism and allows us to formulate a revised scheme incorporating aspects of both previous proposals (Figure 7C). In this mechanism Lys176 acts as the general acid/base for catalysis. On binding ketopantoate, the Lys176 side chain must undergo a conformational change, such that it can hydrogen bond to the C2 carbonyl of the substrate. This residue can then protonate the developing negative charge on ketopantoate. After hydride transfer, the reprotonation of Lys176 from solvent would disrupt the interaction between this residue and pantoate, allowing the release of the product and the return of the lysine side chain to its observed, resting state.

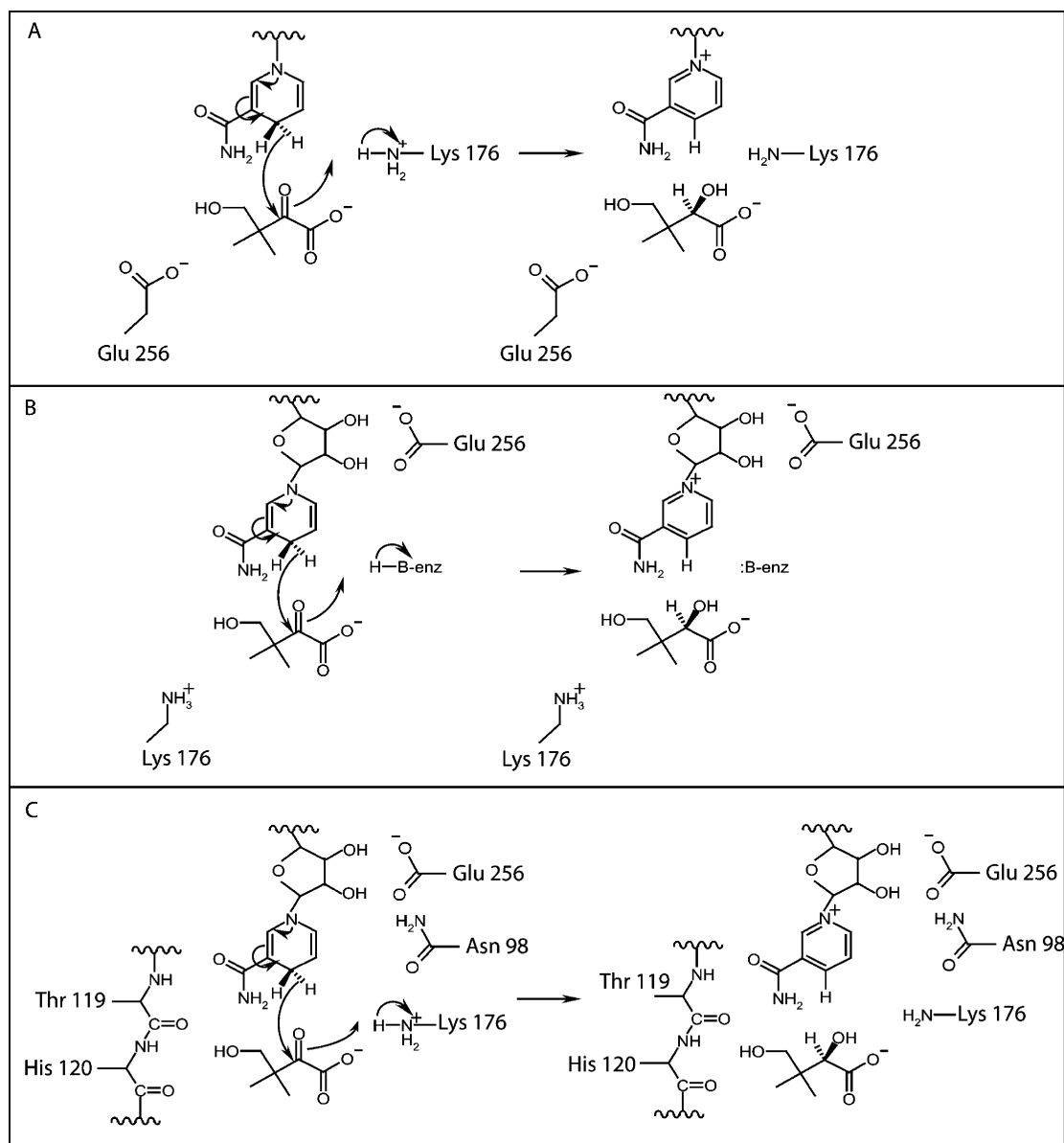


FIGURE 7: Proposed mechanisms of KPR. (A) Mechanism proposed by Zheng et al. (11) on the basis of mutagenesis data. (B) Mechanism proposed by Matak-Vinkovic et al. (14) based on the crystal structure of apo KPR. (C) Revised mechanism proposed on the basis of the binary complex structure and model of the ternary complex in this paper.

The switch between the observed “resting” state of Lys176 and the proposed active conformation relies on the breaking of an interaction with the semiconserved Thr117 to allow an interaction with ketopantoate. The comparison of the apo KPR and KPR–NADP⁺ complex structures reveals subtle differences in the residues surrounding Thr117. This may be to facilitate the change in conformation required for catalysis.

Rather than interacting directly with ketopantoate, Glu256 forms two hydrogen bonds to the nicotinamide ribose of NADP⁺, orienting the cofactor so that it binds to the backbone NH of Ala122, facing the top of the active site cleft. Since ketopantoate binding is significantly improved by the presence of NADPH, it is now clear why the E256A mutation reduced substrate binding (12).

This mechanism provides a role for Asn98. Not only does it form hydrogen bonds to the nicotinamide ribose C2 and C3 hydroxyls of the cofactor, it also hydrogen bonds to either the C1 carboxylic acid or the C2 carbonyl of ketopantoate

and may form a hydrogen bond to the active conformation of Lys176. With the potential to stabilize the substrate, the cofactor, and the key catalytic residue, Lys176, Asn98 is central to the catalytic reaction.

The ternary complex model presented here also implicates the semiconserved residues Thr119 and His120 in stabilizing ketopantoate via interactions with the C4 hydroxyl. The backbone amide and carbonyl of these residues, respectively, can form hydrogen bonds with the substrate.

CONCLUSIONS

KPR plays a key role in the synthesis of pantothenate. This paper reports the structural and thermodynamic characterization of cofactor binding to the enzyme, providing useful insight into the mechanism of the enzyme. Our results have confirmed the importance of Lys176 and Glu256 and identified a central role for Asn98 in the KPR reaction. The structure of the KPR–NADP⁺ complex has been used to derive a model for the ternary complex, which has addition-

ally highlighted the importance of other residues, including Thr117, Thr119, and His120.

ACKNOWLEDGMENT

We thank Professor Diana Downs, Department of Bacteriology, University of Wisconsin—Madison, for supplying the *S. typhimurium* DM 3498 strain. Dr. Dima Chirgadze gave assistance with crystal optimization and X-ray data collection.

SUPPORTING INFORMATION AVAILABLE

Two movie files of normal mode molecular dynamics simulations (Dynamite http://s12-ap550.biop.ox.ac.uk/dynamite_html): PORCUPINE.mpg and EIGENMOVI-E.mpg. This material is available free of charge via the Internet at <http://pubs.acs.org>.

REFERENCES

- Tahiliani, A. G., and Beinlich, C. J. (1991) Pantothenic acid in health and disease, *Vitam. Horm.* **46**, 165–228.
- Brown, G. M. (1959) The metabolism of pantothenic acid, *J. Biol. Chem.* **234**, 370–378.
- Begley, T. P., Kinsland, C., and Strauss, E. (2001) The biosynthesis of coenzyme A in bacteria, *Vitam. Horm.* **61**, 157–171.
- Cronan, J. E., Jr., Littell, K. J., and Jackowski, S. (1982) Genetic and biochemical analyses of pantothenate biosynthesis in *Escherichia coli* and *salmonella typhimurium*, *J. Bacteriol.* **149**, 916–922.
- King, H. L., Jr., Dyar, R. E., and Wilken, D. R. (1974) Ketopantoyl lactone and ketopantoic acid reductases. Characterization of the reactions and purification of two forms of ketopantoyl lactone reductase, *J. Biol. Chem.* **249**, 4689–4695.
- Wilken, D. R., King, H. L., Jr., and Dyar, R. E. (1975) Ketopantoic acid and ketopantoyl lactone reductases. Stereospecificity of transfer of hydrogen from reduced nicotinamide adenine dinucleotide phosphate, *J. Biol. Chem.* **250**, 2311–2314.
- Primerano, D. A., and Burns, R. O. (1983) Role of acetohydroxy acid isomeroreductase in biosynthesis of pantothenic acid in *Salmonella typhimurium*, *J. Bacteriol.* **153**, 259–269.
- Shimizu, S., Kataoka, M., Chung, M., and Yamada, H. (1988) Ketopantoic acid reductase of *Pseudomonas maltophilia* 845. Purification, characterization, and role in pantothenate biosynthesis, *J. Biol. Chem.* **263**, 12077–12084.
- Prody, M. E., and Downs, D. (1998) Apba, the ketopantoate reductase enzyme of *Salmonella typhimurium* is required for the synthesis of thiamine via the alternative pyrimidine biosynthetic pathway, *J. Biol. Chem.* **273**, 5572–5576.
- Prody, M. E., and Downs, D. (1998) The panE gene, encoding ketopantoate reductase, maps at 10 min and is allelic to Apba in *Salmonella typhimurium*, *J. Bacteriol.* **180**, 4757–4759.
- Zheng, R., and Blanchard, J. S. (2000) Identification of active site residues in *E. coli* ketopantoate reductase by mutagenesis and chemical rescue *Biochemistry* **39**, 16244–16251.
- Zheng, R., and Blanchard, J. S. (2000) Kinetic and mechanistic analysis of the *E. coli* panE-encoded ketopantoate reductase, *Biochemistry* **39**, 3708–3717.
- Zheng, R., and Blanchard, J. S. (2003) Substrate specificity and kinetic isotope effect analysis of the *Escherichia coli* ketopantoate reductase, *Biochemistry* **42**, 11289–11296.
- Matak-Vinkovic, D., Vinkovic, M., Saldanha, S. A., Ashurst, J. L., von Delft, F., Inoue, T., Miguel, R. N., Smith, A. G., Blundell, T. L., and Abell, C. (2001) Crystal structure of *Escherichia coli* ketopantoate reductase at 1.7 Å resolution and insight into the enzyme mechanism, *Biochemistry* **40**, 14493–15000.
- Downs, D. M., and Petersen, L. (1994) Apba, a new genetic locus involved in thiamine biosynthesis in *Salmonella typhimurium*, *J. Bacteriol.* **176**, 4858–4864.
- Sambrook, J., Fritsch, E. F., and Maniatis, T. (1989) *Molecular cloning: A laboratory manual*, 2nd ed., Cold Spring Harbor Laboratory Press, New York.
- Rhodes, G. (2000) *Crystallography made crystal clear*, 2nd ed., Academic Press, San Diego.
- Otwinowski, Z., and Minor, W. (1997) in *Methods in enzymology* (Carter, C. W., Jr., and Sweet, R. M., Eds.) pp 307–326, Academic Press, New York.
- Navaza, J. (1994) AMoRe: An automated package for molecular replacement, *Acta Crystallogr. A* **50**, 157–163.
- Navaza, J. (2001) Implementation of molecular replacement in AMoRe *Acta Crystallogr., Sect. D: Biol. Crystallogr.* **57**, 1367–1372.
- Collaborative Computational Project (1994) The ccp4 suite: Programs for protein crystallography, *Acta Crystallogr., Sect. D: Biol. Crystallogr.* **50**, 760–763.
- Brunker, A. T., Adams, P. D., Clore, G. M., DeLano, W. L., Gros, P., Grosse-Kunstleve, R. W., Jiang, J. S., Kuszewski, J., Nilges, M., Pannu, N. S., Read, R. J., Rice, L. M., Simonson, T., and Warren, G. L. (1998) Crystallography & NMR system: A new software suite for macromolecular structure determination *Acta Crystallogr., Sect. D: Biol. Crystallogr.* **54** (Part 5), 905–921.
- McRee, D. E. (1999) Xtalview/xfit—a versatile program for manipulating atomic coordinates and electron density, *J. Struct. Biol.* **125**, 156–165.
- Murshudov, G. N., Vagin, A. A., and Dodson, E. J. (1997) Refinement of macromolecular structure by the maximum-likelihood method, *Acta Crystallogr., Sect. D: Biol. Crystallogr.* **53**, 240–255.
- Kleywegt, G. J., and Jones, T. A. (1998) Databases in protein crystallography, *Acta Crystallogr., Sect. D: Biol. Crystallogr.* **54**, 1119–1131.
- Schüttelkopf, A. W., and van Aalten, D. M. F. (2004) Prodr: A tool for high-throughput crystallography of protein–ligand complexes, *Acta Crystallogr., Sect. D: Biol. Crystallogr.* **60**, 1355–1363.
- Carr, H. Y., and Purcell, E. M. (1954) Effects of diffusion on free precession in nuclear magnetic resonance experiments, *Phys. Rev.* **94**, 630–638.
- Piotto, M., Saudek, V., and Sklenar, V. (1992) Gradient-tailored excitation for single-quantum NMR spectroscopy of aqueous solutions, *J. Biomol. NMR* **2**, 661–665.
- Dalvit, C., Pevarello, P., Tato, M., Veronesi, M., Vulpatti, A., and Sundstrom, M. (2000) Identification of compounds with binding affinity to proteins via magnetization transfer from bulk water, *J. Biomol. NMR*.
- Wiseman, T., Williston, S., Brandts, J. F., and Lin, L. N. (1989) Rapid measurement of binding constants and heats of binding using a new titration calorimeter, *Anal. Biochem.* **179**, 131–137.
- Turnbull, W. B., and Daranas, A. H. (2003) On the value of ΔC_p : Can low affinity systems be studied by isothermal titration calorimetry?, *J. Am. Chem. Soc.* **125**, 14859–14866.
- Barrett, C. P., Hall, B. A., and Noble, M. E. M. (2005) Dynamite: A simple way to gain insight into protein motions, *Acta Crystallogr., Sect. D: Biol. Crystallogr.* (in press).
- Suhre, K., and Sandejaouand, Y. H. (2004) Elnemo: A normal mode web-server for protein movement analysis and the generation of templates for molecular replacement, *Nucleic Acids Res.* **32**, W610–W614.
- Fraczkiewicz, R., and Braun, W. (1998) Exact and efficient analytical calculation of the accessible surface areas and their gradients for macromolecules *J. Comput. Chem.* **19**, 319–333.
- Kleiger, G., and Eisenberg, D. (2002) GXXXG and GXXXA motifs stabilize FAD and NAD(P)-binding Rossmann folds through C(α)-H···O hydrogen bonds and van der Waals interactions, *J. Mol. Biol.* **323**, 69–76.
- Kleiger, G., Grothe, R., Mallick, P., and Eisenberg, D. (2002) GXXXG and AXXXA: Common alpha-helical interaction motifs in proteins, particularly in extremophiles, *Biochemistry* **41**, 5990–5997.
- Hajduk, P. J., Olejniczak, E. T., and Fesik, S. W. (1997) One-dimensional relaxation- and diffusion-edited NMR methods for screening compounds that bind to macromolecules, *J. Am. Chem. Soc.* **119**, 12257–12261.
- Colonna-Cesari, F., Perahia, D., Karplus, M., Eklund, H., Braden, C. I., and Tapia, O. (1986) Interdomain motion in liver alcohol dehydrogenase. Structural and energetic analysis of the hinge bending mode, *J. Biol. Chem.* **261**, 15273–15280.

39. Lamzin, V. S., Dauter, Z., Popov, V. O., Harutyunyan, E. H., and Wilson, K. S. (1994) High-resolution structures of holo and apo formate dehydrogenase, *J. Mol. Biol.* 236, 759–785.
40. Branden, C. I., and Eklund, H. (1980) Structure and mechanism of liver alcohol dehydrogenase, lactate dehydrogenase and glyceraldehyde-3-phosphate dehydrogenase, *Experientia, Suppl.* 36, 40–84.
41. Chandra, N. R., Muirhead, H., Holbrook, J. J., Bernstein, B. E., Hol, W. G., and Sessions, R. B. (1998) A general method of domain closure is applied to phosphoglycerate kinase and the result compared with the crystal structure of a closed conformation of the enzyme, *Proteins* 30, 372–380.
42. Stoll, V. S., Kimber, M. S., and Pai, E. F. (1996) Insights into substrate binding by D-2-ketoacid dehydrogenases from the structure of *Lactobacillus pentosus* D-lactate dehydrogenase, *Structure* 4, 437–447.
43. Brooks, B., and Karplus, M. (1985) Normal modes for specific motions of macromolecules: Application to the hinge-bending mode of lysozyme, *Proc. Natl. Acad. Sci. U.S.A.* 82, 4995–4999.
44. Cooper, A. (1999) Thermodynamic analysis of biomolecular interactions, *Curr. Opin. Chem. Biol.* 3, 557–563.
45. Spolar, R. S., and Record, J. (1994) Coupling of local folding to site-specific binding of proteins to DNA, *Science* 263, 777–784.
46. Perozzo, R., Jelesarov, I., Bosshard, H. R., Folkers, G., and Scapozza, L. (2000) Compulsory order of substrate binding to herpes simplex virus type 1 thymidine kinase—a calorimetric study, *J. Biol. Chem.* 275, 16139–16145.
47. Lovell, S. C., Davis, I. W., Arendall, W. B., III, de Bakker, P. I., Word, J. M., Prisant, M. G., Richardson, J. S., and Richardson, D. C. (2003) Structure validation by calpha geometry: Phi,psi and cbeta deviation, *Proteins* 50, 437–450.

BI0502036